PTEP

Prog. Theor. Exp. Phys. **2025** 013G01 (19 pages)
DOI: 10.1093/ptep/ptae185

Half-Integer Random Resonance Compensation for Further Beam Power Ramp-up in the 3-GeV Rapid Cycling Synchrotron of the Japan Proton Accelerator Research Complex

Kunihiro Kojima*, Hiroyuki Harada, Fumihiko Tamura, Hidefumi Okita, Motoki Chimura, and Pranab Kumar Saha

J-PARC Center, Japan Atomic Energy Agency (JAEA), Tokai, Ibaraki 319-1995, Japan
*Email: kunihiro.kojima@j-parc.jp

Received September 4, 2024; Revised December 2, 2024; Accepted December 9, 2024; Published December 10, 2024

A comprehensive study on random resonances was conducted to mitigate beam losses and ensure sufficient tunability of the operating point for further beam power ramp-up in the 3-GeV rapid cycling synchrotron of the Japan Proton Accelerator Research Complex. Low-intensity beam studies revealed considerable excitation of the half-integer random resonance. This half-integer random resonance was successfully compensated for using trim quadrupole magnets without exciting other higher-order resonances. By implementing a conventional theoretical procedure based on resonance driving terms, we identified the leakage field from extraction magnets as the primary source of the error field driving the random resonance. High-intensity beam studies confirmed that our resonance compensation approach substantially mitigated beam loss in higher-tune regions, making it highly effective in improving operating point tunability.

Subject Index G02, G10, G11

1. Introduction

The 3-GeV rapid cycling synchrotron (RCS) serves as a high-intensity and high-brightness proton driver within the accelerator chain of the Japan Proton Accelerator Research Complex (J-PARC), as detailed in Table 1 [1]. The RCS accelerates an injected proton beam from 400 MeV up to 3 GeV at a repetition rate of 25 Hz, delivering it to the downstream Material and Life Science Experimental Facility (MLF) and Main Ring (MR) synchrotron. The RCS employs a multiturn charge exchange injection scheme utilizing a carbon stripper foil [2]. A schematic of the RCS is shown in Fig. 1, while its beta and dispersion functions are shown in Fig. 2. As shown in Figs. 1 and 2, the RCS features a 3-fold symmetric lattice, with each superperiod comprising one arc section and one dispersion-free straight section.

Since its beam commissioning in October 2007, the RCS has undergone progressive improvements in its beam power ramp-up [3–7]. In 2019, it achieved a design output beam power of 1 MW. We are now advancing the beam power ramp-up, aiming to surpass this design output. In megawatt-class high-power proton machines, beam losses can result in high levels of radioactivity, potentially restricting the available beam power. Although the current beam loss in the

© The Author(s) 2024. Published by Oxford University Press on behalf of the Physical Society of Japan. This is an Open Access article distributed under the terms of the Creative Commons Attribution License (https://creativecommons.org/licenses/by/4.0/), which permits unrestricted reuse, distribution, and reproduction in any medium, provided the original work is properly cited.

Downloaded from https://academic.oup.com/ptep/article/2025/1/013G01/7920793 by guest on 07 March 2025

Table 1. Basic parameters of the RCS.

Circumference	348.333 m
Number of cells	27
Superperiod (N_{sp})	3
Operating point (ν_x, ν_y)	(6.46, 6.36)
Injection energy	400 MeV
Extraction energy	3 GeV
Design output beam power	1 MW
Momentum spread	±1%
Natural chromaticity (horizontal/vertical)	−9.1/−6.9
Controlled chromaticity (horizontal/vertical)	−8.0/−9.7
Ring acceptance	486π mm·mrad
Collimator aperture	324π mm·mrad
Painting area	200π mm·mrad (MLF) 50π mm·mrad (MR)
Injection period	0.5 ms
Injection turns	307
Harmonic number	2
Number of bunches	2
Number of particles per pulse	8.3×10^{13}

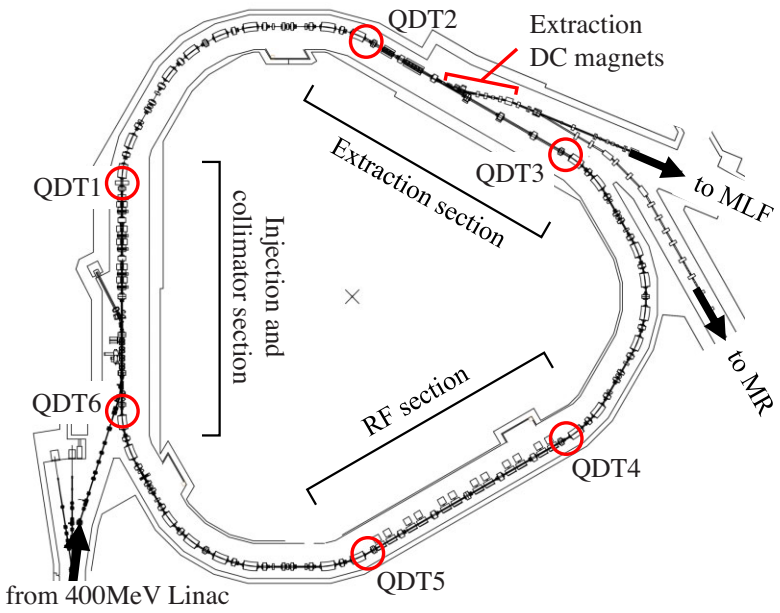

Fig. 1. Schematic of the RCS. Red circles indicate the locations of the QDTs. QDT, trim quadrupole magnet; RF, radio frequency.

RCS has been successfully minimized to 0.1% at the design beam power of 1 MW [8], further reductions in beam loss are necessary to realize the ongoing beam power ramp-up.

In the low-energy region of the RCS, the space-charge effect becomes particularly important regarding beam loss mitigation [9–16]. To minimize this effect, the RCS adopts transverse injection painting [4,17–20]. The RCS also adopts longitudinal injection painting. This technique involves creating a momentum offset to the RF bucket and controlling a second harmonic RF to flatten the particle density [5,21–23]. However, as beam power increases with the ongoing

Downloaded from https://academic.oup.com/ptep/article/2025/1/013G01/7920793 by guest on 07 March 2025

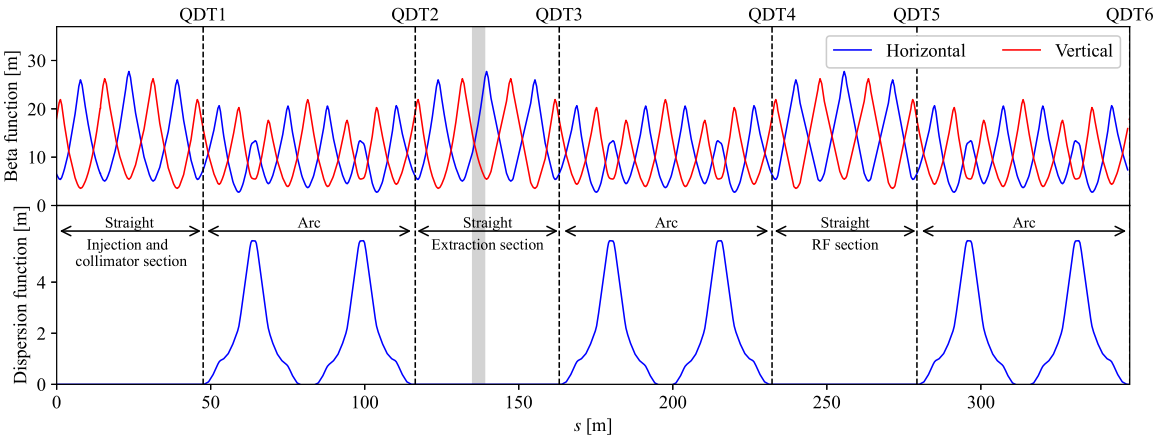

Fig. 2. Beta and dispersion functions along the RCS. Black dashed lines indicate the positions of the QDTs, while the gray-shaded area indicates the beam transport line adjacent to the extraction DC magnets.

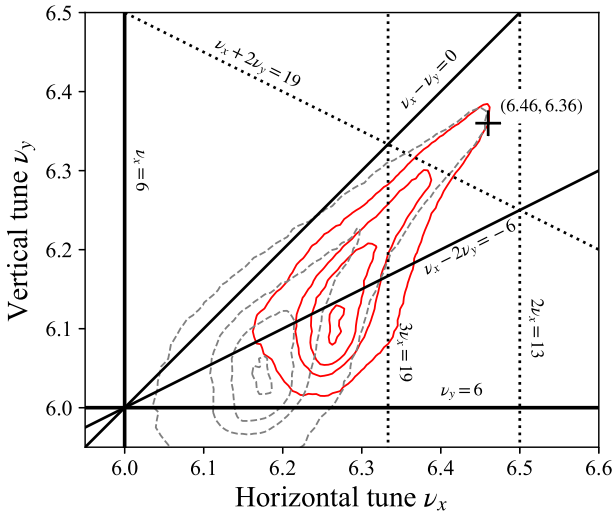

Fig. 3. Tune footprints immediately after multiturn injection for output beam powers of 1 MW (red solid curves) and 1.5 MW (gray dashed curves). Resonance lines up to the third order are plotted in black. Solid lines represent structure resonances, whereas dotted lines represent random resonances.

ramp-up, the space-charge effect becomes increasingly pronounced. This is problematic because repulsive forces between particles extend the tune footprint toward structure resonances ($\nu_{x(y)} = 6$), as shown in Fig. 3. When the tune footprint crosses these resonances, the beam quality may deteriorate, leading to unacceptable beam losses. To avoid such resonance crossing of the tune footprint, shifting the operating point to a higher-tune region is essential. On the other hand, previous studies on high-intensity beams indicate that the tunability of the operating point is inadequate. Consequently, even minor shifts in the operating point can result in substantial beam losses (see the black curves in Fig. 20 given later).

In addition to the space-charge effect, the large amount of the chromatic tune shift is one of the key issues. Since the sextupole magnets are devoted to compensating for the third-order structure resonance $\nu_x - 2\nu_y = -6$, the chromaticity cannot be fully corrected. Moreover, the absence of full chromaticity correction is preferable in suppressing the beam instability [24,25]. The RCS features a momentum acceptance of $\pm 1\%$, resulting in a horizontal- and vertical-

Downloaded from https://academic.oup.com/ptep/article/2025/1/013G01/7920793 by guest on 07 March 2025

chromaticity-induced tune shift of approximately 0.1. This shift requires a resonance-free region that is wide enough to accommodate the majority of particles. Furthermore, chromaticity can induce a positive tune shift, potentially leading to resonance crossing above the operating point in the tune space. The aforementioned chromaticity-induced tune spread complicates the identification of the resonance contributing predominantly to the beam loss.

To enhance the tunability of the operating point for beam power ramp-up, we conducted a comprehensive resonance study. Given that the operations of the MLF primarily influence the residual radiation in the RCS, due to the higher beam duty of the MLF compared with that of the MR, this study predominantly focused on the beam intended for the MLF. Initially, we examined the half-integer random resonance $2\nu_x = 13$, which is positioned just above the current operating point $(\nu_x, \nu_y) = (6.46, 6.36)$ and is speculated to most critically influence the tunability of the operating point in higher-tune regions. Compensating for the resonance $2\nu_x = 13$ is likely a major step toward our goal of surpassing the 1-MW output beam power. Note that, unlike previous studies that exclusively discuss resonance crossing of a high-intensity beam below the operating point due to the space-charge-induced negative tune shift [26–32], our main concern is resonance crossing above the operating point due to the chromaticity-induced positive tune shift. The remainder of this paper is structured as follows: Section 2 begins with our study on the resonance $2\nu_x = 13$. Subsequently, we discuss the compensation of this resonance using trim quadrupole magnets, namely, QDTs. Section 2.3 focuses on the excitation of third-order random resonances due to the addition of the QDTs. Section 3 is dedicated to high-intensity beam studies under the same user-operation beam conditions. Finally, Section 4 presents a summary of our findings.

2. Low-intensity beam studies

Given that the excitation of random resonances is fundamentally determined based on the lattice structure, we performed several low-intensity beam studies. Specifically, by utilizing a low particle density, the effects of the space-charge-induced tune spread were minimized, allowing us to concentrate on beam losses resulting from lattice imperfections.

2.1. *Excitation of the half-integer random resonance*

To investigate the primary cause of the limited tunability of the operating point, we first investigated the effect of the half-integer random resonance $2\nu_x = 13$. Figure 4 shows the injection beam profiles used for this study. The beam was injected into the RCS in a single turn with an intensity of 0.3 kW-eq. (5.0×10^{10} particles per pulse). To focus on the resonance in the horizontal direction, the beam was injected with an offset corresponding to the painting area $\varepsilon_{p,x}$ in the horizontal direction, while the vertical offset was set to zero. Furthermore, to replicate the conditions leading to chromatic-tune-shift-induced resonance crossing, the beam was injected with a momentum offset of -0.35% relative to the synchronized particle along the longitudinal direction. For simplicity, the second radio frequency (RF) harmonic was deactivated, simplifying the synchrotron motion of particles into an almost simple harmonic oscillation.

The operating point for the RCS was set at $(\nu_x, \nu_y) = (6.46, 6.36)$, which matches the current operational setting used for the MLF. Throughout the acceleration process, spanning 20 ms, this operating point was shifted following a certain pattern. Figure 5 shows the typical tune tracking pattern. As shown in this figure, the horizontal operating tune shifts to lower values, effectively moving away from the resonance $2\nu_x = 13$. Accordingly, resonance-induced beam losses are

Downloaded from https://academic.oup.com/ptep/article/2025/1/013G01/7920793 by guest on 07 March 2025

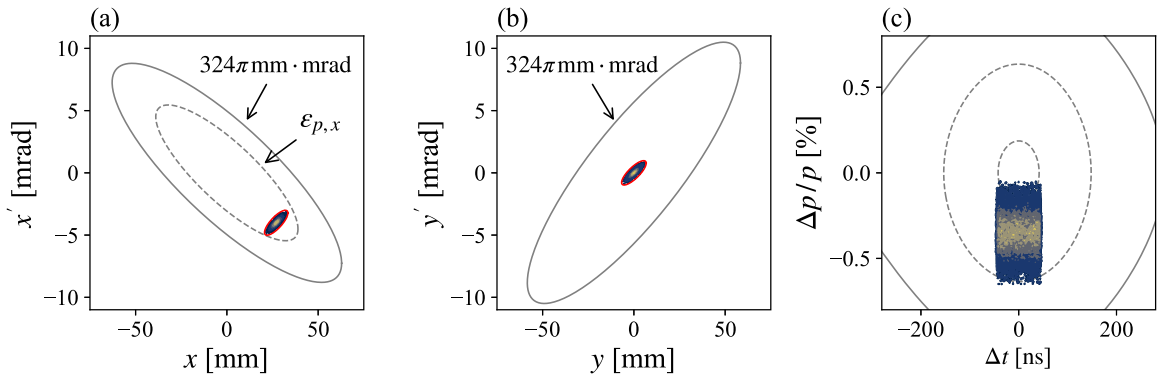

Fig. 4. Schematic of injection beam profile. (a), (b), and (c) depict the horizontal, vertical, and longitudinal phase spaces, respectively. Furthermore, the separatrices corresponding to the painting area $\varepsilon_{p,x}$ (dashed curve) and collimator aperture (solid curves) are plotted in (a) and (b), respectively. The dashed and solid curves shown in (c) represent the separatrix and acceptance, respectively.

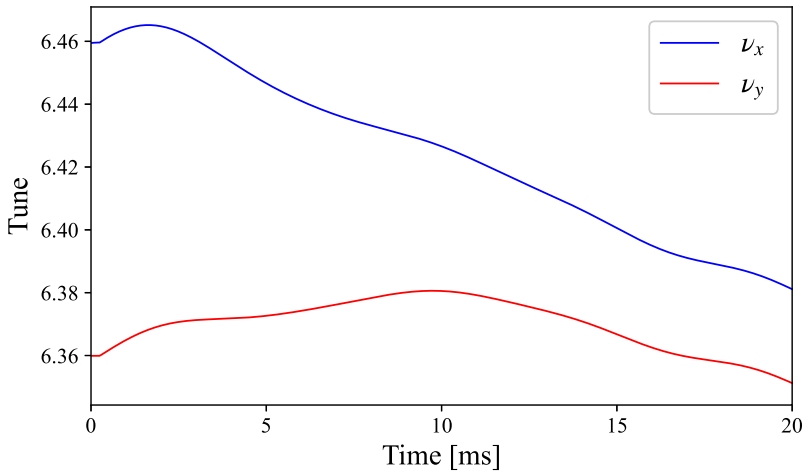

Fig. 5. Example of the time evolutions of horizontal (blue) and vertical (red) tunes.

speculated to be severe during injection and the early stages of acceleration. Therefore, we focus on the beam loss occurring over the first 4 ms after injection.

The numerical simulation results obtained with "Simpsons" [33,34] for a horizontal painting area of $\varepsilon_{p,x} = 200\pi$ mm·mrad are shown in Fig. 6. The corresponding numerical simulation does not consider space-charge force due to the low beam intensity. The present parameters of the RCS excluding the lattice imperfections are incorporated in the simulation. The nonlinear components up to the tenth order such as the sextupole magnet and fringe fields are also incorporated. To enhance the resonance $2\nu_x = 13$, an additional quadrupole field with a strength of approximately 0.1% of the strength of the main quadrupole magnets is assumed. Figure 6(b) shows that particles affected by the resonance experience severe beta beating, causing their amplitudes to exceed the collimator aperture. This results in a periodic increase in the number of lost particles corresponding to the synchrotron oscillation, as shown in Fig. 6(c).

Figure 7(a) shows the beam loss monitor (BLM) signals measured at the collimator section. These signals resemble the simulation results shown in Fig. 6(c). Notably, the amplitude of the BLM signals depends on the energies of lost particles and is not proportional to the number of lost particles. Similar signals are observed by most other BLMs. This consistency indicates

Downloaded from https://academic.oup.com/ptep/article/2025/1/013G01/7920793 by guest on 07 March 2025

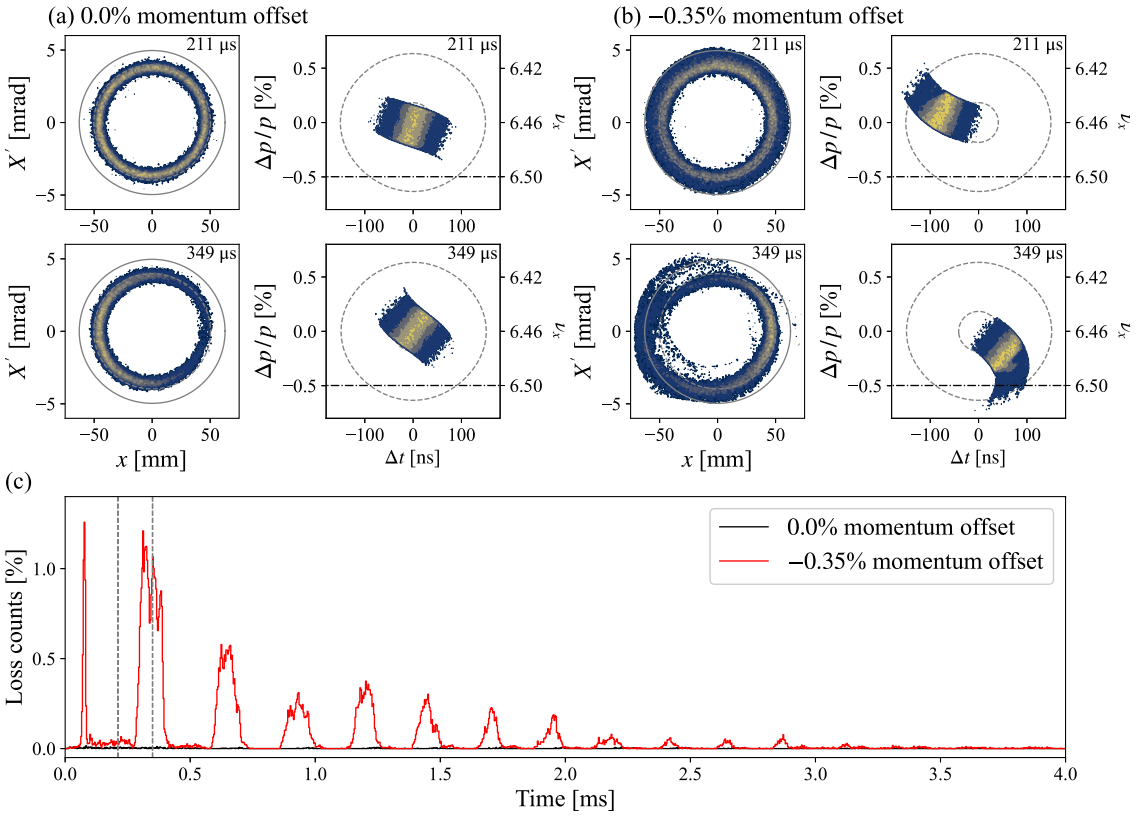

Fig. 6. Simulation results obtained for the horizontal painting area of $\varepsilon_{p,x} = 200\pi$ mm·mrad. (a) and (b) The horizontal and longitudinal phase spaces, with X' defined to make the distribution upright relative to the x–x' plane. The horizontal and longitudinal phase spaces with (a) no momentum offset and (b) momentum offset of -0.35% at 211 and 349 μs after injection are shown. The definitions of the gray curves presented in (a) and (b) are identical to those assumed for the case presented in Fig. 4(a) and (c). (c) The time evolution of the beam loss. The gray dashed lines correspond to the phase spaces shown in (a) and (b).

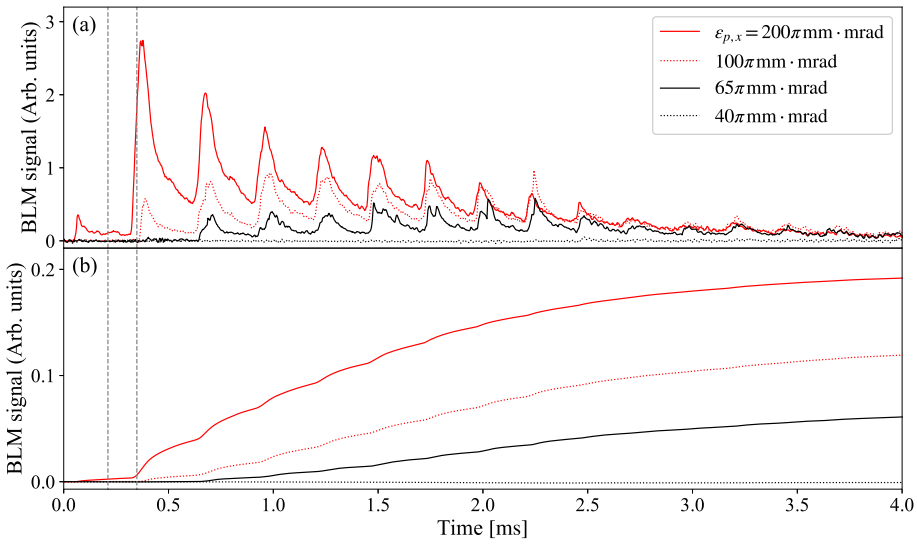

Fig. 7. (a) BLM signals measured over the first 4 ms at the collimator section for four injection painting areas in the horizontal plane and (b) their integrations. The definitions of the gray dotted lines are identical to those presented in Fig. 6(c).

Downloaded from https://academic.oup.com/ptep/article/2025/1/013G01/7920793 by guest on 07 March 2025

considerable excitation of the resonance $2\nu_x = 13$. The excitation of this random resonance suggests the presence of an error field that disrupts the 3-fold symmetry of the RCS.

Next, we evaluated the effect of the resonance on transverse beam acceptance. In the RCS, the beam painting area $\varepsilon_{p,x}$ can be changed arbitrarily [17,35]. Figure 7(b) shows the integrated curves of the BLM signals for four painting areas in the horizontal plane: $\varepsilon_{p,x} = 40$, 65, 100, and 200π mm·mrad. Considerable beam losses were observed for all painting areas except for $\varepsilon_{p,x} = 40\pi$ mm·mrad, and these beam losses increased with increasing painting areas, indicating that particularly for off-momentum particles in low-intensity beams, the horizontal acceptance of the RCS around the operating point $(\nu_x, \nu_y) = (6.46, 6.36)$ is substantially reduced by the half-integer resonance. Therefore, compensating for the resonance $2\nu_x = 13$ is crucial for achieving broader tunability and beam power ramp-up.

2.2. *Definition of the half-integer random resonance driving term*

The excitation and compensation of the half-integer random resonance can be analyzed by using the resonance driving term (RDT). When we consider the effect of a small lattice imperfection, the single-particle Hamiltonian of the transverse motion subject to a perturbation can be written as

$$\begin{aligned} H(x, y, x', y'; s) &= H_0 + \delta V, \\ H_0 &= \frac{x'^2 + y'^2}{2} + \frac{k_x(s)x^2 + k_y(s)y^2}{2}, \end{aligned} \tag{1}$$

where the independent variable s is the path length along the design beam orbit, δV represents the perturbation driving random resonances, and H_0 represents the unperturbed Hamiltonian. k_x and k_y represent s-dependent functions determined by the lattice structure. Assuming a linear perturbation of $\delta V = \kappa_1(s)(x^2 - y^2)/2$, where $\kappa_1(s)$ is the s-dependent function reflecting lattice imperfections, the RDT for the half-integer random resonance $2\nu_x = 13$ is given by

$$\Delta G_{2,0,13} = \frac{1}{4\pi} \oint \beta_x(s)\kappa_1(s) e^{j[2\chi_x(s) - (2\nu_x - 13)\theta]} ds, \tag{2}$$

where $\beta_x(s)$ is the unperturbed beta function, $\chi_x = \int^s ds/\beta_x(s)$, and j is imaginary. θ is the scaled independent variable and given by $\theta = 2\pi s/L$, where L is the circumference of the RCS. Assuming that the error field is localized within a narrow area along the ring, Eq. (2) is then approximated to be

$$\Delta G_{2,0,13} \approx \frac{1}{4\pi} \beta_x(s_0) K_1 e^{j[2\chi_x(s_0) - (2\nu_x - 13)\theta_0]}, \tag{3}$$

where K_1 is the integral of $\kappa_1(s)$ over the area, and s_0 represents the position of the quadrupole field of K_1. The resonance compensation is equal to making the amplitude of the RDT zero, and it is achieved by canceling the RDT origin from the error field with the additional linear field.

2.3. *Compensation of the half-integer random resonance*

In the RCS, the QDT is a promising component that is available for resonance compensation. All QDTs belong to a specific type of defocusing quadrupole magnet, with six QDTs arranged at both ends of each straight section, as illustrated in Figs. 1 and 2. These QDTs can be independently excited using six independent unipolar power sources. Figure 8(c) shows the typical excitation pattern of QDTs. The power sources currently used for the RCS are not capable of

Downloaded from https://academic.oup.com/ptep/article/2025/1/013G01/7920793 by guest on 07 March 2025

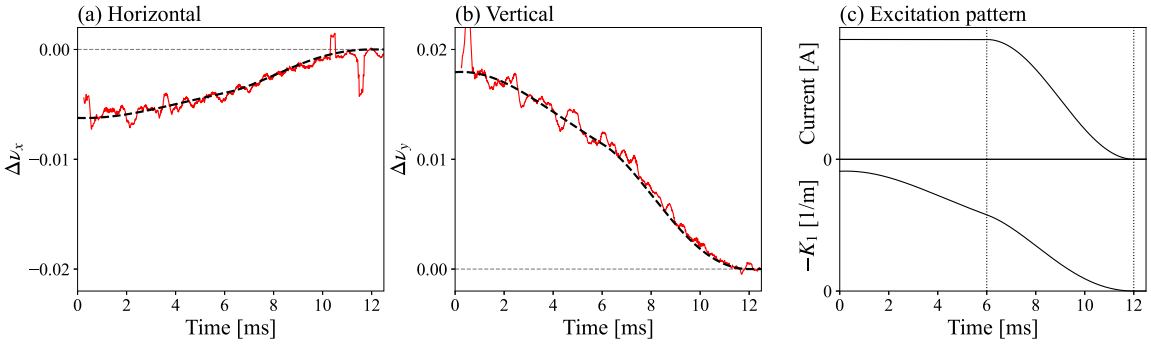

Fig. 8. Time evolutions of the (a) horizontal and (b) vertical tune shifts enhanced by the excitation of QDT1 with a peak current of 100 A. (c) Typical excitation pattern of QDTs. The black dashed curves shown in (a) and (b) represent fitting results.

supporting the entire 20-ms acceleration process. Hence, the excitation current of each QDT is maintained constant for the first 6 ms, then gradually decreased, and finally lowered to zero after 12 ms. Correspondingly, the quadrupole strength continues to ramp with magnetic rigidity, as shown in the lower plot of Fig. 8(c).

To improve the estimation of the quadrupole strength of the QDTs, we conducted a beam-based correction of the excitation curve. For this, we adopted a method allowing for high-accuracy measurements of tunes [36]. This correction procedure based on the tune shift is among the most reliable procedures. Figure 8(a) and (b) show examples of the tune shifts enhanced by the excitation of QDT1 with a peak current of 100 A. As long as the tune shift is not so large, the tune shifts $\Delta\nu_x$ and $\Delta\nu_y$ are well approximated by

$$\Delta\nu_x = \frac{\beta_x(s_0)K_1}{4\pi}, \qquad \Delta\nu_y = -\frac{\beta_y(s_0)K_1}{4\pi}. \tag{4}$$

Here, s_0 corresponds to the position of the QDT. The optical functions of the RCS have already been corrected [3,17]. Based on the optics correction and measurements, the horizontal and vertical beta functions for the position of QDT1 are assumed to be $\beta_x(s_0) = 6.74$ and $\beta_y(s_0) = 17.3$ m, respectively, for the first 6 ms. The excitation curve is expressed as $K_1 = C_1 I/B\rho$, where $B\rho$ represents the magnetic rigidity, I represents the excitation current, and C_1 is a constant. By fitting the tune shifts from 1 to 5 ms, as shown in Fig. 8(a) and (b), we obtain $C_1 = -3.8 \times 10^{-4} \pm 0.4 \times 10^{-4}$ T/A for the horizontal tune shift and $-4.07 \times 10^{-4} \pm 0.19 \times 10^{-4}$ T/A for the vertical tune shift. Thus, the evaluated C_1 values for the horizontal and vertical directions are consistent. Corrections for the excitation curve were also conducted for other QDTs, yielding the same result. Thus, a C_1 value of -4.0×10^{-4} T/A was adopted in this study.

Figure 9 shows the direction of the RDT of each QDT in the complex plane. Each RDT points along a different direction compared with the others, indicating that any error field can be compensated for by exciting two QDTs without using a bipolar power source. To confirm the effect of the resonance compensation using QDTs, we conducted a beam study. Then, a difficulty lies in the quantitative evaluation of the resonance excitation using the BLM, since the modulation of betatron beating driven by the QDT addition made the beam loss location shift upstream or downstream. This leads to an increase or decrease in the BLM signal unrelated to resonance excitation or compensation as shown in Fig. 10. One can see that the responses of

Downloaded from https://academic.oup.com/ptep/article/2025/1/013G01/7920793 by guest on 07 March 2025

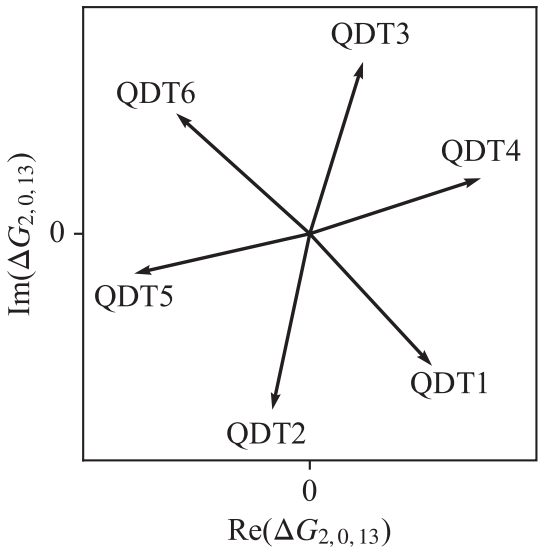

Fig. 9. Comparison of the RDTs, obtained using Eq. (3), for all QDTs. The abscissa and ordinate represent the real and imaginary parts, respectively, of each RDT.

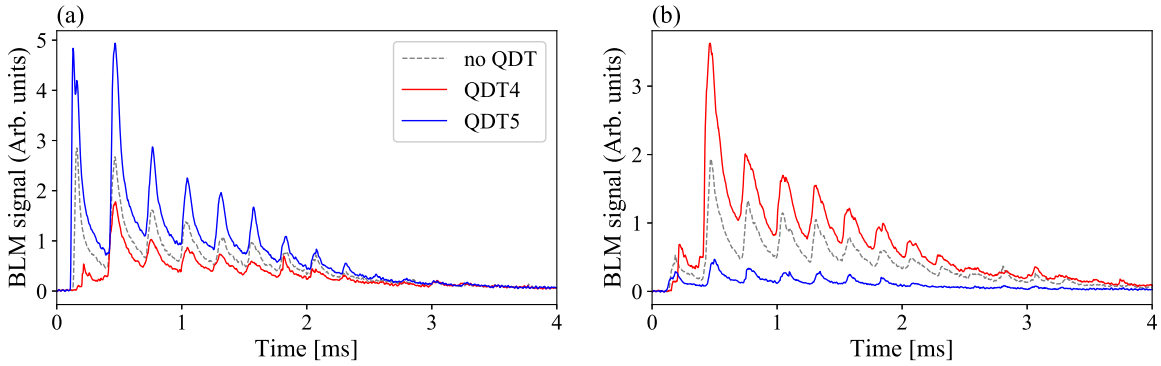

Fig. 10. The signals measured with (a) the BLM of Fig. 7 and (b) a BLM installed 7.4 m upstream of (a). The horizontal painting area was set at 200π mm·mrad, and the other beam conditions are the same as employed in Fig. 7. Red, blue, and gray dashed curves correspond to cases involving the addition of QDT4, addition of QDT5, and absence of QDTs, respectively. QDT4 or QDT5 was excited with a peak current of 30 A.

the two BLM signals to the addition of QDTs are opposite, even though the two BLMs are only 7.4 m apart from each other. Thus, a DC current transformer (DCCT) was used instead of the BLM to evaluate the excitation of the resonance through particle survival rate measurements.

Figure 11 shows the beam profiles immediately after beam injection in this case. The beam was injected with an offset corresponding to the painting area $\varepsilon_{p,x}$ of 120π mm·mrad in the horizontal direction, while the vertical offset was set to zero. The beam intensity was increased to 5 kW-eq. (8.3×10^{11} particles per pulse) to compensate for the low sensitivity of the DCCT to beam loss; beam was injected within 30 turns every 2 turn steps. Furthermore, the beam was injected without a momentum offset along the longitudinal direction to mitigate the chromatic tune shift for simplicity.

Figure 12 shows the particle survival rates corresponding to the case wherein the operating point is set at $(\nu_x, \nu_y) = (6.49, 6.36)$, which is speculated to be within the resonant stopband of $2\nu_x = 13$. In this case, the QDTs were excited with peak currents of 30 A. The survival

Downloaded from https://academic.oup.com/ptep/article/2025/1/013G01/7920793 by guest on 07 March 2025

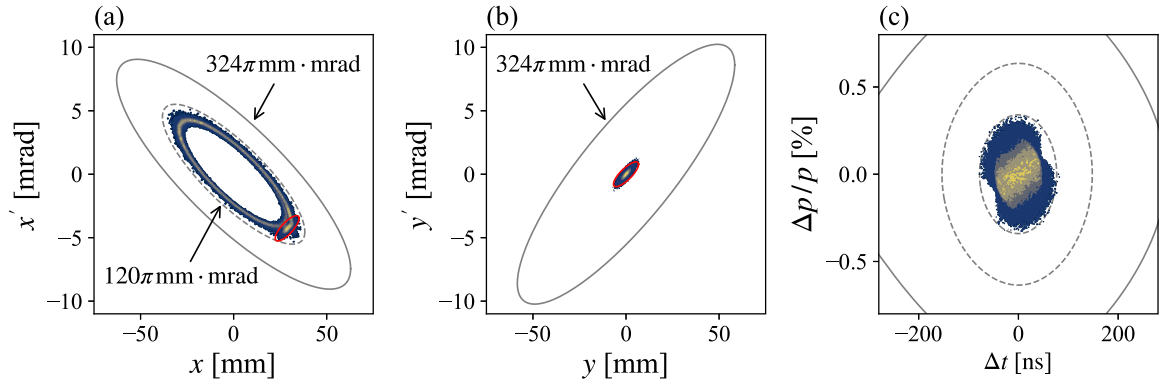

Fig. 11. Schematic of injection beam profile. The meanings of each plot and definitions of the gray curves are identical to those assumed for the case presented in Fig. 4.

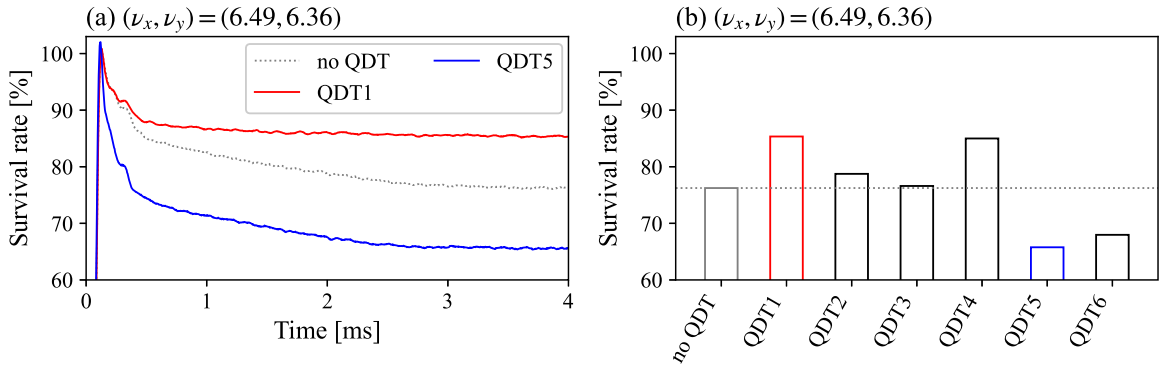

Fig. 12. (a) Time evolution of particle survival rates over the first 4 ms after injection. Red, blue, and black curves correspond to cases involving the addition of QDT1, addition of QDT6, and absence of QDTs, respectively. (b) Particle survival rates after 4 ms with the independent addition of each of the six QDTs. The excitation peak currents of the QDTs were set to 30 A in all cases, excluding that with no QDT.

rates differed clearly depending on the excited QDT, as shown in Fig. 12(b). Considering the symmetric positioning of the QDTs, the observed differences in survival rates are attributed to the excitation or compensation of the resonance $2\nu_x = 13$. Furthermore, the variations in the survival rate are consistent with the directions of the RDTs shown in Fig. 9. For instance, the addition of QDT1 or QDT4 reduces beam loss, whereas the addition of QDT5 or QDT6, with RDTs in nearly opposite directions, increases beam loss. This indicates that QDTs can be effectively used for compensating the resonance $2\nu_x = 13$.

Next, to experimentally determine the optimal excitation currents for the QDTs that minimize resonance-induced beam losses from $2\nu_x = 13$, survival rate mapping was performed. Two QDTs were essential and sufficient for this purpose. QDT1 and QDT4 were selected because their addition mitigated beam losses more effectively compared with the addition of other QDTs, as shown in Fig. 12. Figure 13 presents the mapping result at the operating point $(\nu_x, \nu_y) = (6.50, 6.36)$. The excitation currents of the two QDTs were converted to the RDT using Eq. (3) and assuming an injection energy of 400 MeV. The maximum survival rate of 92% was observed when the excitation peak currents for QDT1 and QDT4 were set at 26.6 and 8.5 A, respectively.

Downloaded from https://academic.oup.com/ptep/article/2025/1/013G01/7920793 by guest on 07 March 2025

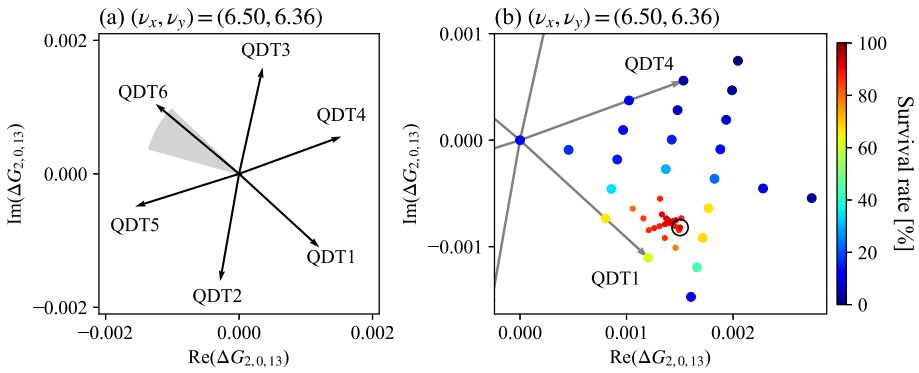

Fig. 13. (a) RDTs for each QDT excited with a peak current of 30 A. (b) Scan of the excitation currents for QDT1 and QDT4. The abscissa and ordinate represent the real and imaginary parts, respectively, of the RDT generated by the addition of the QDTs at an injection energy of 400 MeV. (a) The gray-shaded area indicates the RDT obtained from the beam transport line adjacent to the extraction DC magnets. (b) Markers are color-coded based on the corresponding survival rate at 4 ms after injection, with the black circle denoting the case when QDT1 and QDT4 are excited with peak currents of 26.6 and 8.5 A, respectively.

The successful compensation of the resonance $2\nu_x = 13$ by adding QDT1 and QDT4 is a critical clue for identifying the primary source of the error field driving $2\nu_x = 13$. This error field should have an RDT directed between the RDTs of QDT3 and QDT6 in the complex plane and whose amplitude is comparable to the compensation field from QDTs. The RDT of the magnetic field difference between each main quadrupole magnet had an amplitude estimated from the measurements as $|G_{2,0,13}| = 2.4 \times 10^{-4}$, which is about one-eighth of that of the QDTs, and hardly likely to be the primary source of the error field. Similarly, the amplitude of the RDT produced by momentum deviation and magnetic field difference between each sextupole magnet is estimated to be only on the order of 10^{-4} compared with that of QDTs. On the other hand, according to Eq. (3), the direction of the RDT is determined by the position of the error field along the RCS. Furthermore, considering that the QDTs were excited with static currents over the first 4 ms after injection, the primary component of the error field is likely static rather than varying with the magnetic rigidity. Hence, the most promising candidate for the required error field is the leakage field from the extraction DC magnets installed along the beam transport line (3NBT) adjacent to the extraction section of the RCS [37, 38], whose RDT is indicated by the gray-shaded area in Fig. 13(a) and is almost opposite to those of QDT1 and QDT4.[1]

Figure 14(b) shows the particle survival rates at 4 ms after injection at each operating point. Here, the horizontal tune was varied from $\nu_x = 6.46$ to 6.55 in steps of 0.01 by controlling the main quadrupole magnets except for the QDTs, while the vertical tune was fixed at $\nu_y = 6.36$. The beam conditions were identical to those presented in Fig. 11. Resonance-induced beam loss was clearly observed near a horizontal tune of 6.50, which corresponds to the resonance condition of $2\nu_x = 13$. The beam loss was considerably mitigated when the extraction DC magnets were deactivated, indicating that $2\nu_x = 13$ is mostly driven by the leakage field from the extraction DC magnets, as expected. However, some beam loss was still observed, likely due to

[1] All injection bump magnets are rapidly deactivated after the beam injection, and their effect on the excitation of the half-integer resonance should be lower than that of the extraction DC magnets, unlike the case of Ref. [32].

Downloaded from https://academic.oup.com/ptep/article/2025/1/013G01/7920793 by guest on 07 March 2025

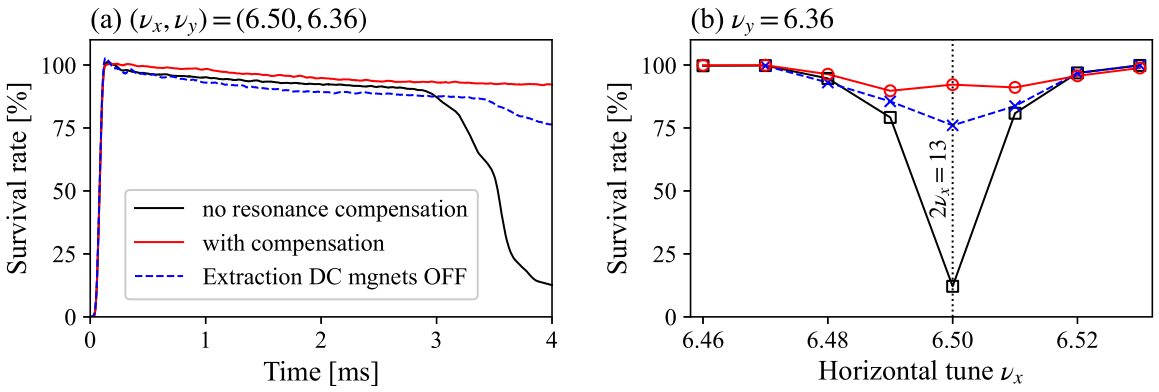

Fig. 14. (a) Time evolution of particle survival rates measured by the DCCT at a tune of $\nu_x = 6.50$. (b) Tune dependence of the particle survival rate 4 ms after beam injection. The vertical tune was set to 6.36 in all cases. Red and black curves show the results with and without QDT-based resonance compensation, respectively, while blue dashed curves show the result obtained by turning off the extraction DC magnets.

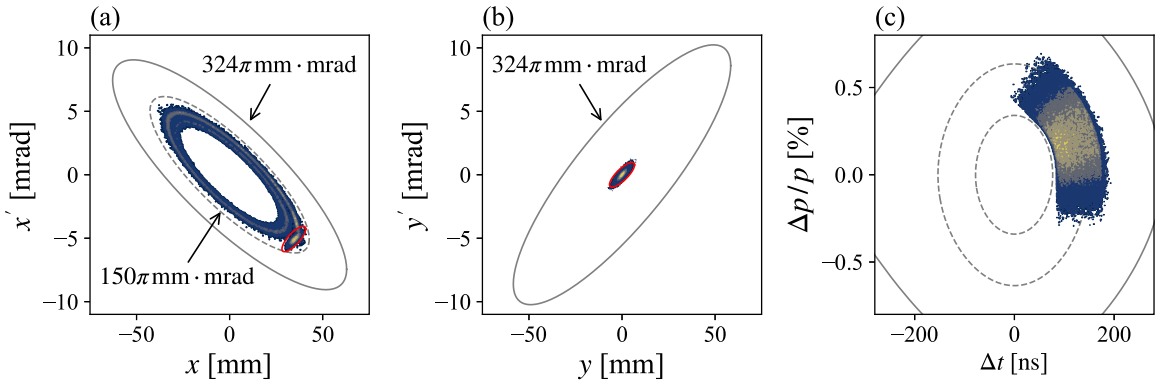

Fig. 15. Schematic of injection beam profile. The meanings of each plot and definitions of the gray curves are identical to those assumed for the case presented in Fig. 4.

the other error fields, indicating that shielding to limit leakage is not a perfect solution. The effectiveness of QDT-based resonance compensation was reconfirmed in Fig. 14. Consequently, the addition of QDTs with appropriate strengths was identified as the optimal solution, even compared to turning off the extraction DC magnets.

The resonance compensation achieved for the on-momentum particle may not be optimal for the case of resonance crossing due to the chromaticity-induced tune shift of the off-momentum particle. Since additional focusing or defocusing that is the cause of the chromatic effect modulates the beta function and phase advance of the off-momentum particle, the RDT for the off-momentum particle differs from that of the on-momentum particle, as is evident from Eq. (3). To address this point, we conducted a beam study dedicated to the off-momentum particles at the operating point of $(\nu_x, \nu_y) = (6.46, 6.36)$. Figure 15 shows the beam profiles immediately after beam injection. Unlike the case of Fig. 11, the beam was injected with a delay of 130 ns, corresponding to a momentum offset of 0.5%, and the horizontal painting area was expanded to 150π mm·mrad to enhance the resonance-induced beam loss. In this case, the particles having momentum deviation of about -0.5% cross $2\nu_x = 13$ due to the chromaticity-induced tune shift. As expected, the optimal excitation peak current for QDT4 that is determined similarly to in Fig. 13 changed from 8.5 A to 3.5 A, and the survival rate was maximized from 95.5% to

Downloaded from https://academic.oup.com/ptep/article/2025/1/013G01/7920793 by guest on 07 March 2025

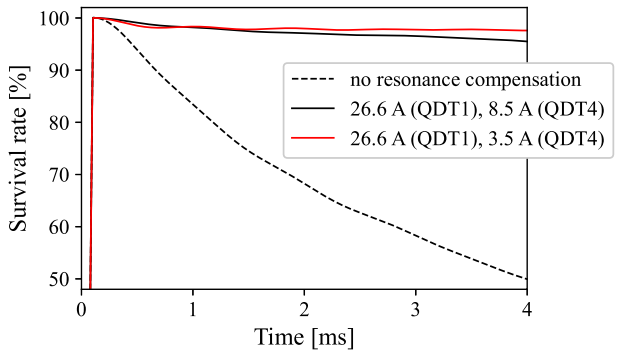

Fig. 16. Time evolution of particle survival rates measured by the DCCT at the operating point of $(\nu_x, \nu_y) = (6.46, 6.36)$. Red and black solid curves show the results with the excitation peak currents for QDT1: both were set at 26.6 A, while QDT4 was excited at a peak current of 3.5 and 8.5 A, respectively. The black dashed curve shows the result obtained without QDT-based resonance compensation.

97.6% as shown in Fig. 16. Consequently, such fine-tuning is preferable to achieve better resonance compensation for the off-momentum particle. In addition, our resonance compensation method based on DCCT was confirmed to work well in the case of the off-momentum particle.

2.4. *Excitation of the third-order random resonance*

Our next study assesses whether the addition of QDTs, which distorts the beta function, excites other random resonances. In particular, our focus is on the third-order resonances, which denote the next higher order to $2\nu_x = 13$. Given that numerous particles cross $3\nu_x = 19$ and $\nu_x + 2\nu_y = 19$ due to space-charge-induced tune shift, exciting these resonances may increase beam loss even if $2\nu_x = 13$ is completely compensated.

Assuming $\delta V = \kappa_2(s)(x^3 - 3xy^2)/6$ in Eq. (1), the RDTs for the third-order resonances are described as

$$\begin{aligned}\Delta G_{3,0,19} &\approx \frac{1}{12\sqrt{2}\pi}\sum_n \hat{\beta}_x^{3/2}(s_n)K_2^n e^{j[3\hat{\chi}_x(s_n)-(3\nu_x-19)\theta_n]},\\ \Delta G_{1,2,19} &\approx \frac{1}{4\sqrt{2}\pi}\sum_n \hat{\beta}_x^{1/2}(s_n)\hat{\beta}_y(s_n)K_2^n e^{j[\hat{\chi}_x(s_n)+2\hat{\chi}_y(s_n)-(\nu_x+2\nu_y-19)\theta_n]}.\end{aligned} \tag{5}$$

Here, the hat denotes modulation due to the compensation of $2\nu_x = 13$, and $\hat{\beta}_x(s)$ and $\hat{\beta}_y(s)$ satisfy the following relation:

$$\begin{aligned}\frac{d^2}{ds^2}\sqrt{\hat{\beta}_x(s)} + [k_x(s) + \kappa_1(s)]\hat{\beta}_x(s) - \frac{1}{\hat{\beta}_x(s)^{3/2}} = 0,\\ \frac{d^2}{ds^2}\sqrt{\hat{\beta}_y(s)} + [k_y(s) - \kappa_1(s)]\hat{\beta}_y(s) - \frac{1}{\hat{\beta}_y(s)^{3/2}} = 0.\end{aligned} \tag{6}$$

Sextupole fields are localized in some areas along the RCS, and n represents the serial number assigned to each area. K_2^n represents the integral of $\kappa_2(s)$ over the nth area, s_n represents the position of the nth area along the RCS, and $\theta_n = 2\pi s_n/L$. The corresponding stopband widths

Downloaded from https://academic.oup.com/ptep/article/2025/1/013G01/7920793 by guest on 07 March 2025

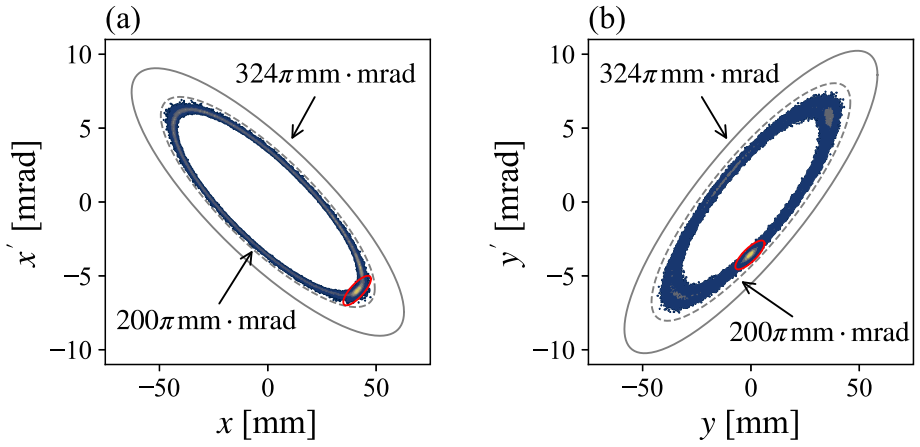

Fig. 17. Schematic of injection beam profile. The meanings of each plot and definitions of the gray curves are consistent with those assumed for the case presented in Fig. 4.

$\delta_{3,0,19}$ and $\delta_{1,2,19}$ satisfy the following relations [39]:

$$\left|\frac{\delta_{3,0,19}}{\Delta G_{3,0,19}}\right| = \frac{3}{2}\sqrt{\frac{A_x}{2}}, \qquad \left|\frac{\delta_{1,2,19}}{\Delta G_{1,2,19}}\right| = \frac{4A_x + A_y}{2\sqrt{2A_x}}, \tag{7}$$

where A_x and A_y are single-particle Courant–Snyder invariants in the horizontal and vertical planes, respectively. For the QDT-addition-based compensation of $2\nu_x = 13$, the calculated RDTs are $|\Delta G_{3,0,19}| = 1.0 \times 10^{-3}$ and $|\Delta G_{1,2,19}| = 2.0 \times 10^{-2}$ m$^{-1/2}$ at an injection energy of 400 MeV. The corresponding stopband widths for outer particles with $A_{x(y)} = 200\pi$ mm·mrad are $\delta_{3,0,19} = 2.2 \times 10^{-5}$ and $\delta_{1,2,19} = 7.1 \times 10^{-4}$, respectively. These widths are found to barely deteriorate beam stability, which is also seen in single-particle tracking.

The excitation of third-order random resonances was evaluated through a low-current beam study. Both horizontal and vertical painting areas were set at 200π mm·mrad (Fig. 17) considering that the beam loss caused by $3\nu_x = 19$ and $\nu_x + 2\nu_y = 19$ will be substantially lower than that caused by $2\nu_x = 13$. Other beam conditions were identical to those in the case of Fig. 11. Figure 18 shows the tune dependence of the particle survival rates measured using the DCCT. The operating point was varied from $(\nu_x, \nu_y) = (6.31, 6.21)$ to $(6.40, 6.30)$. Despite increasing the excitation peak current of QDT1 to 60 A, the resonance $\nu_x + 2\nu_y = 19$ was detected with almost no beam loss. This indicates that this resonance minimally affects beam loss. Furthermore, a considerable beam loss of approximately 20% was observed near the resonance line of $3\nu_x = 19$. As shown in Fig. 18, QDT excitation resulted in only a 2% increase in the beam loss at $\nu_x = 6.33$. Hence, the compensation of the resonance $2\nu_x = 13$ exerts an acceptable effect on the excitation of third-order random resonances.

3. High-intensity beam studies

We conducted a high-intensity beam study to demonstrate the effectiveness of resonance compensation in mitigating beam loss and improving tunability. The study used the same beam conditions as those for MLF user operations, with a beam intensity of 1 MW-eq. (8.24×10^{13} particles per pulse). Figure 19 shows the progress of multiturn beam injection simulated using

Downloaded from https://academic.oup.com/ptep/article/2025/1/013G01/7920793 by guest on 07 March 2025

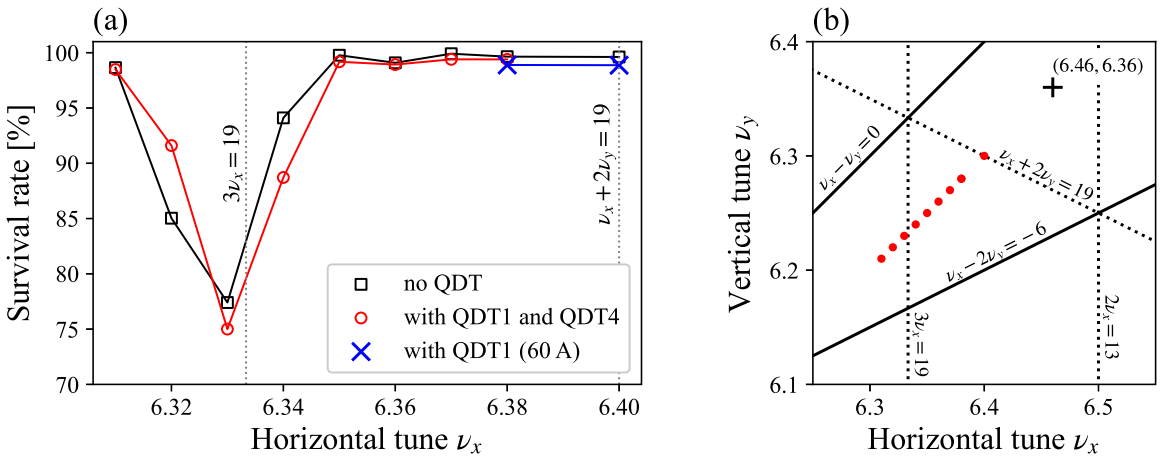

Fig. 18. (a) Beam survival rate 4 ms after injection as a function of the horizontal tune. Red and black curves show the results obtained with and without QDT1 and QDT4 addition, with excitation peak currents of 26.6 and 8.5 A, respectively. The blue cross indicates the case wherein QDT1 is excited with a peak current of 60 A. (b) Red dots denote the operating points used in this beam study.

Simpsons. The tune footprints shown in the left column of Fig. 19 are affected by the chromaticity effect, space charge force, and external nonlinear force. In the early stages of injection, the tune footprint overlaps with $2\nu_x = 13$ due to chromatic effects. As beam intensity increases, the repulsive space-charge force pushes the tune footprint to a lower value, causing it to move away from the $2\nu_x = 13$ resonance by the 100th turn. By the end of injection, the beam achieves a uniform distribution in real space, along both the horizontal and vertical planes. The painting area is set to 200π mm·mrad in both planes [20]. Furthermore, the beam density is flattened along the longitudinal direction through longitudinal painting.

Figure 20 shows the BLM signals measured at the collimator section over the first 4 ms after injection. Because the relative beam loss is considered extremely small for measurement using the DCCT, we used the BLM. Here, QDT1 and QDT4 were excited with optimized peak currents of 26.6 and 8.5 A, respectively. The maximum tune shifts caused by the addition of the QDTs were only -2.2×10^{-3} and 5.9×10^{-3} along the horizontal and vertical directions, respectively, negligibly impacting beam loss. Notably, the beam loss observed before 500 μs primarily resulted from foil hitting during injection and is beyond the scope of the present study [5,40,41].

Contrary to our expectations, Fig. 20(a) shows a marginal increase in the beam loss with QDT addition at the operating point $(\nu_x, \nu_y) = (6.46, 6.36)$; a similar tendency is observed for most BLMs. Moreover, the changes in the excitation currents for QDT1 and QDT4 of several amperes hardly affect the beam loss. This indicates that particles do not approach $2\nu_x = 13$ due to space-charge effects, which is consistent with the results presented in Fig. 19(c), where the tune footprint has already moved away from $2\nu_x = 13$ before the horizontal painting area reaches 65π mm·mrad. Furthermore, the absence of a considerable increase in beam loss indicates that the addition of QDTs barely excites any other resonances.

While Fig. 20(a) indicates minimal improvement, panel (b) demonstrates a substantial reduction in beam loss by a factor of approximately 3 with QDT addition. The difference between panels (a) and (b) is attributed to the change in the position of the operating point from $(\nu_x, \nu_y) = (6.46, 6.36)$ to $(6.49, 6.36)$. As shown in Fig. 20(b), resonance-induced beam loss and

Downloaded from https://academic.oup.com/ptep/article/2025/1/013G01/7920793 by guest on 07 March 2025

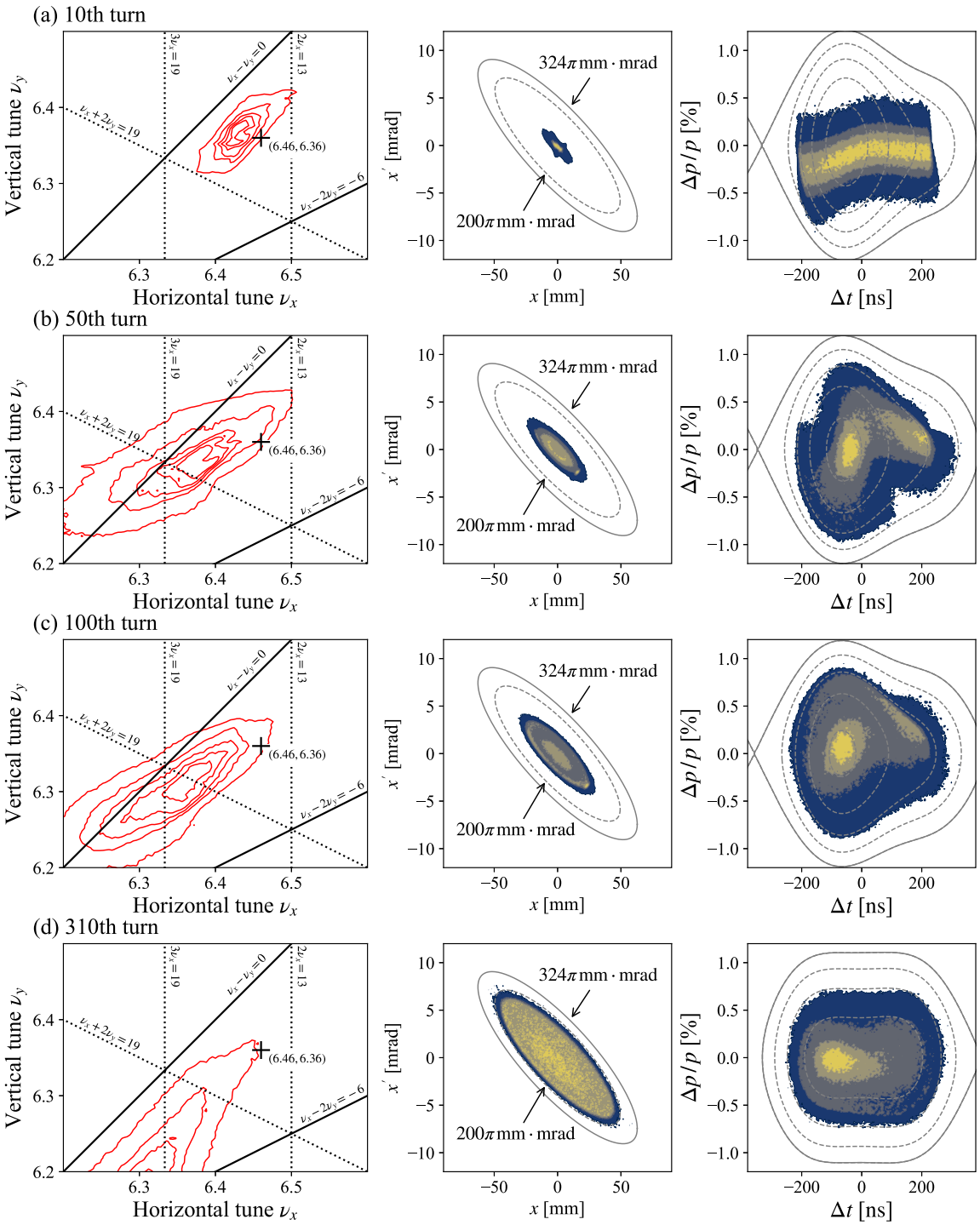

Fig. 19. Tune footprints (left) and horizontal (center) and longitudinal (right) phase spaces at the (a) 10th, (b) 50th, (c) 100th, and (d) 310th turn computed using Simpsons. The definitions of the gray curves in these phase spaces are identical to those assumed for the case presented in Fig. 4.

the effects of compensation increased as the operating point approached $2\nu_x = 13$. This result suggests that compensating $2\nu_x = 13$ is considerably effective in mitigating beam loss in the higher-tune region and improving tunability. The definitive reason for the beam loss increase in Fig. 20(b) with the resonance compensation compared to (a) has not been identified yet but will be revealed in future studies. On the other hand, QDT excitation is currently limited by

Downloaded from https://academic.oup.com/ptep/article/2025/1/013G01/7920793 by guest on 07 March 2025

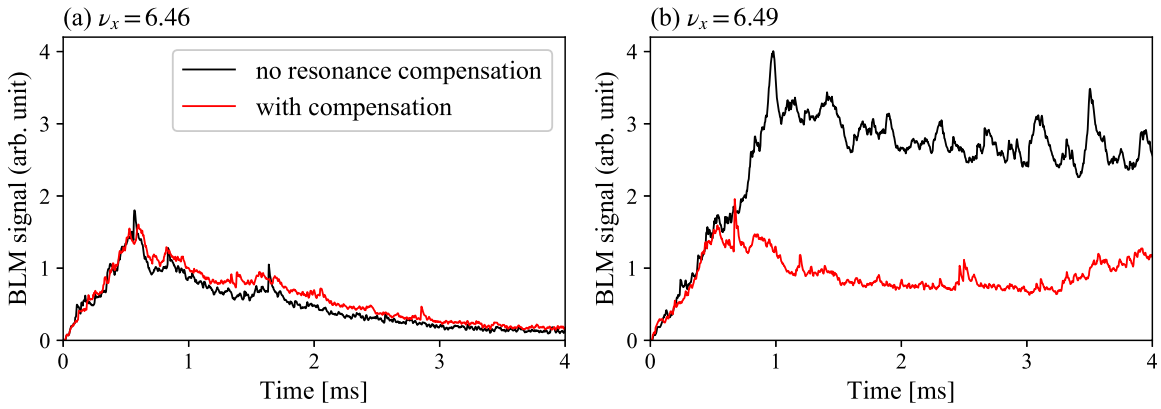

Fig. 20. BLM signals measured at the collimator section over the first 4 ms at operating points (a) $(\nu_x, \nu_y) = (6.46, 6.36)$ and (b) (6.49, 6.36). Red and black curves show the results corresponding to QDT addition and no QDT addition, respectively.

the performance of power sources, which can only accommodate corrections for up to 6 ms from the beginning of injection. This limitation results in the interruption of the resonance compensation if a horizontal operating tune exceeding 6.49 is selected.

4. Summary

Random resonances in the J-PARC RCS were investigated to enhance the tunability of the operating point in preparation for beam power ramp-up. Low-intensity beam studies revealed that the transverse acceptance of 324π mm·mrad deteriorated to less than 65π mm·mrad for off-momentum particles due to the excitation of $2\nu_x = 13$. We achieved the successful mitigation of the resonance with QDTs in low-intensity beam studies. Based on RDT analysis, we identified the extraction DC magnets on the 3NBT as the most likely source of the error field driving $2\nu_x = 13$. This theoretical prediction was confirmed through measurements wherein the extraction DC magnets were deactivated. Furthermore, we examined third-order random resonances, finding that QDT addition for $2\nu_x = 13$ compensation minimally affected the excitation of the resonances $3\nu_x = 19$ and $\nu_x + 2\nu_y = 19$. High-intensity beam studies further validated the effectiveness of this resonance compensation. The results revealed that at the current operating point $(\nu_x, \nu_y) = (6.46, 6.36)$, QDT addition did not adversely affect beam stability. At the operating point (6.49, 6.36), $2\nu_x = 13$ compensation considerably mitigated beam loss to approximately one-third, demonstrating the feasibility of tunability improvement.

Based on these promising outcomes, our focus has now shifted to the exploration of higher-tune regions and the realization of output beam powers beyond design specifications. Our primary concern is the timing delay observed when the beam crosses $2\nu_x = 13$. In this case, the QDT-based resonance compensation method must remain valid; the excitation currents of the QDTs can be optimized to minimize beam loss during resonance crossing (Section 2). Once we resolve the limitations imposed by QDT power sources, we expect to achieve adequate operating point tunability for beam power ramp-up.

Acknowledgements

The authors are grateful to the J-PARC RCS, linac, MR, and 3NBT group members for their indispensable support during the beam experiment. We are also grateful to Dr. M. Kinsho, Dr. K. Yamamoto, Dr. J. Kamiya, and Dr. M. Yamamoto for their continuous support and encouragement for the present work.

Downloaded from https://academic.oup.com/ptep/article/2025/1/013G01/7920793 by guest on 07 March 2025

The authors wish to thank Prof. H. Hotchi for his valuable advice, helpful discussions, and support for the Simpsons simulations. The authors would like to acknowledge the help of Dr. S. Hatakeyama, Dr. Y. Watanabe, Dr. I. Yamada, and Mr. S. Nagayama for the beam experiment.

References

[1] Accelerator Group, JAERI/KEK Joint Project Team, "Accelerator Technical Design Report for J-PARC", 2003. JAERI: Ibaraki. KEK-Report 2002-13 and JAERI-Tech 2003-044.
[2] I. Sugai, Y. Takeda, M. Oyaizu, H. Kawakami, Y. Irie, A. Takagi, H. Hattori, and K. Kawasaki, Nucl. Instrum. Methods Phys. Res. A Accel. Spectrom. Detect. Assoc. Equip. **613**, 457 (2010).
[3] H. Hotchi et al., Phys. Rev. ST Accel. Beams **12**, 040402 (2009).
[4] H. Hotchi et al., Phys. Rev. ST Accel. Beams **15**, 040402 (2012).
[5] H. Hotchi et al., Prog. Theor. Exp. Phys. **2012**, 02B003 (2012).
[6] H. Hotchi et al., Phys. Rev. ST Accel. Beams **20**, 060402 (2017).
[7] H. Hotchi et al., J. Instrum. **15**, P07022 (2020).
[8] P. K. Saha et al., Proc. 15th Int. Part. Accel. Conf. (IPAC'24), eds. Pilat F., Fischer W., Saethre R., Anisimov P., and Andrian I. (JACoW Publishing, Geneva, 2024), p. 939.
[9] J. A. Holmes, V. V. Danilov, J. D. Galambos, D. Jeon, and D. K. Olsen, Phys. Rev. ST Accel. Beams **2**, 114202 (1999).
[10] J. D. Galambos, S. Danilov, D. Jeon, J. A. Holmes, D. K. Olsen, F. Neri, and M. Plum, Phys. Rev. ST Accel. Beams **3**, 034201 (2000).
[11] S. Cousineau, S. Y. Lee, J. A. Holmes, V. Danilov, and A. Fedotov, Phys. Rev. ST Accel. Beams **6**, 034205 (2003).
[12] H. Hotchi, Phys. Rev. Accel. Beams **23**, 050401 (2020).
[13] T. Yasui, S. Igarashi, Y. Sato, T. Koseki, and K. Ohmi, Phys. Rev. Accel. Beams **23**, 061001 (2020).
[14] J. Eldred, V. Lebedev, K. Seiya, and V. Shiltsev, Phys. Rev. Accel. Beams **24**, 044001 (2021).
[15] J. Holmes, T. Gorlov, N. Evans, M. Plum, and S. Cousineau, Phys. Rev. Accel. Beams **21**, 124403 (2018).
[16] T. Yasui and Y. Kurimoto, Phys. Rev. Accel. Beams **25**, 121001 (2022).
[17] H. Harada, PhD thesis (KEK Preport 2009-7), Graduate School of Science, Hiroshima University, Higashihiroshima, Hiroshima (2009).
[18] P. K. Saha, Y. Shobuda, H. Hotchi, N. Hayashi, T. Takayanagi, H. Harada, and Y. Irie, Phys. Rev. ST Accel. Beams **12**, 040403 (2009).
[19] P. K. Saha et al., Phys. Rev. ST Accel. Beams **16**, 120102 (2013).
[20] P. K. Saha, M. Yoshimoto, S. Hatakeyama, H. Hotchi, H. Harada, F. Tamura, K. Yamamoto, Y. Yamazaki, M. Kinsho, and Y. Irie, Phys. Rev. Accel. Beams **3**, 082801 (2020).
[21] F. Tamura et al., Phys. Rev. ST Accel. Beams **12**, 041001 (2009).
[22] M. Yamamoto et al., Nucl. Instrum. Methods Phys. Res. A Accel. Spectrom. Detect. Assoc. Equip. **621**, 15 (2010).
[23] P. K. Saha et al., Phys. Rev. Accel. Beams **21**, 024203 (2018).
[24] P. K. Saha et al., Proc. 7th Int. Part. Accel. Conf. (IPAC'16), eds. Petit-Jean-Genaz C., Kim D. E., Ko I. S., Kim K. R., and Schaa V. R. W. (JACoW Publishing, Geneva, 2016), p. 589.
[25] Y. Shobuda et al., Prog. Theor. Exp. Phys. **2017**, 013G01 (2017).
[26] F. J. Sacherer, PhD thesis (Lawrence Radiation Lab Report UCRL-18454), University of California, Berkeley, CA (1968).
[27] R. L. Gluckstern, Proc. Linear Accel. Conf. 1970 (LINAC70), ed. M. Tracy (National Accelerator Laboratory, Batavia, IL, 1970), p. 811.
[28] I. Hofmann and K. Beckert, IEEE Trans. Nucl. Sci. **32**, 2264 (1985).
[29] S. Machida, Nucl. Instrum. Methods Phys. Res. A Accel. Spectrom. Detect. Assoc. Equip. **309**, 43 (1991).
[30] R. Baartman, AIP Conf. Proc. **448**, 56 (1998).
[31] A. V. Fedotov and I. Hofmann, Phys. Rev. ST Accel. Beams **5**, 024202 (2002).
[32] Y. Li, Y. S. Yuan, S. Y. Xu, Y. W. An, X. H. Lu, and S. Wang, Phys. Rev. Accel. Beams **26**, 104201 (2023).
[33] S. Machida, AIP Conf. Proc. **297**, 459 (1993).
[34] S. Machida and M. Ikegami, AIP Conf. Proc. **448**, 73 (1998).

Downloaded from https://academic.oup.com/ptep/article/2025/1/013G01/7920793 by guest on 07 March 2025

[35] T. Takayanagi, J. Kamiya, M. Watanabe, Y. Yamazaki, Y. Irie, J. Kishiro, I. Sakai, and T. Kawakubo, IEEE Trans. Appl. Supercond. **16**, 1358 (2006).
[36] H. Harada and N. Hayashi, Proc. 3rd J-PARC Symposium (J-PARC2019), ed. Endo H. (Physical Society of Japan (JPS), Tokyo, 2021), 011027.
[37] M. Yoshimoto et al., Proc. 11th European Particle Accelerator Conf. (EPAC) 2008, eds. Andrian I., and Petit-Jean-Genaz C. (JACoW Publishing, Geneva, 2008), p. 3626.
[38] J. Kamiya, N. Ogiwara, H. Hotchi, N. Hayashi, and M. Kinsho, Nucl. Instrum. Methods Phys. Res. A Accel. Spectrom. Detect. Assoc. Equip. **763**, 329 (2014).
[39] E. D. Courant and H. S. Snyder, Ann. Phys. (N.Y.) **3**, 1 (1958).
[40] K. Yamamoto and S. Kato, Phys. Rev. ST Accel. Beams **15**, 120401 (2012).
[41] S. Kato, K. Yamamoto, M. Yoshimoto, H. Harada, and M. Kinsho, Phys. Rev. ST Accel. Beams **16**, 071003 (2013).

Downloaded from https://academic.oup.com/ptep/article/2025/1/013G01/7920793 by guest on 07 March 2025

© The Author(s) 2024. Published by Oxford University Press on behalf of the Physical Society of Japan. This is an Open Access article distributed under the terms of the Creative Commons Attribution License (https://creativecommons.org/licenses/by/4.0/), which permits unrestricted reuse, distribution, and reproduction in any medium, provided the original work is properly cited.